Acta Materialia 107 (2016) 229–238

Contents lists available at ScienceDirect

Acta Materialia

journal homepage: www.elsevier.com/locate/actamat

Full length article

# Blind source separation aided characterization of the γ′ strengthening phase in an advanced nickel-based superalloy by spectroscopic 4D electron microscopy

David Rossouw*, Robert Krakow, Zineb Saghi [2], Catriona S.M. Yeoh, Pierre Burdet [1], Rowan K. Leary, Francisco de la Peña, Caterina Ducati, Catherine M.F. Rae, Paul A. Midgley

*Department of Materials Science and Metallurgy, University of Cambridge, 27 Charles Babbage Road, Cambridge, CB3 0FS, UK*

ARTICLE INFO

*Article history:*
Received 24 September 2015
Received in revised form
15 December 2015
Accepted 20 January 2016
Available online 12 February 2016

ABSTRACT

The γ′ strengthening phase in an advanced nickel-based superalloy, ATI 718Plus, was characterized using a blind source separation applied to a four dimensional X-ray microanalysis dataset obtained by scanning transmission electron microscopy. Selected patterns in the X-ray spectra identified by independent component analysis were found to be spatially and chemically representative of the matrix (γ) and precipitate phases (γ′) present in the superalloy, enabling their size, shape and distribution to be determined. The three dimensional chemical reconstruction of the microstructure may provide insight into the role of the various alloying elements in the evolution of the microstructure at the nano-scale.



## 1. Introduction

ATI 718Plus® (718Plus) is an advanced nickel-based superalloy that has been developed for use in aircraft and gas turbine engines. The high strength superalloy is the product of extensive efforts to increase the operation temperature of its predecessor, the widely used alloy 718, to 718 + 100 °F, without sacrificing its excellent processability and relatively low cost in comparison with other high temperature superalloys [1]. Despite comprising a dozen or more alloying elements, the salient microstructures of nickel-based superalloys are relatively simple, consisting of a dense dispersion of γ′ precipitates in a nickel-base γ matrix. The 718Plus superalloy also contains a blocky η phase containing niobium (Ni6Nb[Al,Ti]) which was not present in the region selected for analysis. The superalloy microstructure, including the size distribution and volume fraction of the γ′ phase, can be carefully controlled by tailored heat treatments. In most nickel-based superalloys, the major contribution to the retention of strength at elevated temperatures is provided by the unusual behavior of $L1_2$ ordered γ′ ($Ni_3Al$) precipitates, whose presence in the microstructure increases dislocation drag, resulting in a considerable increase in flow stress with increasing temperature [2]. Given the pivotal role the ordered γ′ phase plays in superalloy metallurgy, and its profound influence on the high temperature strength and creep resistance of nickel superalloys, it is of vital importance to characterize the size, shape, volume fraction and composition of the γ′ phase to better understand the structure-property relationships in superalloys. Here, we use a novel combination of electron tomography, spectroscopy and machine learning techniques to characterize a 718Plus superalloy, providing access to 3D spatially resolved chemical information at the nanoscale.

The investigation of fine-scale microstructural features inherent in superalloys demands an analytical materials characterization technique capable of nanometer spatial resolution. The 3D atom-probe tomography (APT) technique has contributed to a deeper understanding of microstructural transformations in superalloys, as well as a better understanding of the relationship between the alloy chemistry, microstructure, and mechanical properties [3]. However, despite some notable strengths, APT has several draw backs: the field evaporation of the material during analysis is destructive, the specimen may break under the high electric fields, atomic resolution can only be attained along the depth scale, the analyzed volume (typically 10 × 10 × 100 $nm^3$) is small, and compositional variations in evaporation fields lead to local magnification artefacts.

* Corresponding author. Present address: Department of Materials Science and Engineering, McMaster University, 1280 Main Street West, Hamilton, ON, L8S 4L1, Canada.
*E-mail address:* rossoud@mcmaster.ca (D. Rossouw).
[1] Present address: École polytechnique fédérale de Lausanne, SB-CIME, Station 12, 1015 Lausanne, Switzerland.
[2] Present address: CEA, LETI, MINATEC Campus, F-38054 Grenoble, France.

http://dx.doi.org/10.1016/j.actamat.2016.01.042

Electron tomography (ET), performed in the transmission electron microscope (TEM), can also be a powerful method for characterizing superalloys, and may be complementary technique to APT because ET is a (nominally) non-destructive technique with an inherently larger field of view. The general principle of ET is to combine mathematically a systematic set of electron microscope images, containing different views of an object, into a 3D reconstruction of the object [4]. For the superalloy sample needle analyzed here, images obtained by high annular dark field scanning transmission electron microscopy (HAADF STEM) of the needle did not contain appreciable compositional contrast. We therefore combined electron tomography and energy-dispersive X-ray (EDX) spectroscopy techniques, entailing so called '4D' microscopy, to analyze the superalloy microstructure, seeking to reconstruct the 3D chemical distribution of the superalloy with nanometer spatial resolution. The proposed method is feasible due to recent advances in instrumentation, including improved X-ray detection efficiency and the use of modern computer systems capable of handling and processing large datasets.

The 3D structural characterization of nanoscale materials by electron tomography is a mature technique in the physical sciences [5,6]. Early examples of 4D spectroscopic characterization [7,8] were limited by low signal collection efficiencies, and only in the last few years has improved instrumentation led to a number of examples of 4D electron microscopy appearing in the literature. Examples include the 3D elemental mapping of a 28 nm metal gate transistor [9], a lithium ion battery cathode [10] hollow metal nanoparticles [11,12], and simultaneous electron energy loss spectroscopy (EELS) and EDX tomography of an Al–Si alloy [13]. Once a 4D dataset is acquired, a number of methods can be used to reconstruct a 3D chemical volume. For example, selected element maps may be reconstructed to obtain 3D element distributions [13], or each energy channel in a spectrum may be reconstructed to obtain a 4D volume with a full spectrum at each voxel [14]. Here, using an alternative approach, we reconstruct a limited number of machine learning derived components to obtain their relative weightings in 3D. Machine learning techniques have been used previously to identify and image different phases in multi-phase materials from 2D projections [15–17]. If the components extracted from a given EDX dataset are physically interpretable, as has been shown recently in the case of core–shell nanostructures [18], and their spatial weightings satisfy the projection requirement, then their reconstruction may provide a simplified and clearer representation of the material's composition.

## 2. Experimental

### 2.1. Materials

The 718Plus material studied was provided by Rolls-Royce Deutschland Ltd. & Co KG (RRD). The initial ingot was triple vacuum melted for high cleanliness and forged into a billet product. The subsequent sub-solvus forging and heat treatment processes were developed by RRD in cooperation with Otto Fuchs KG: Pre-solution: 843 °C–871 °C/16 h, Solution: 954 °C–982 °C/1 h and Aging: 788 °C/2 h–8 h/FC + 704 °C/8 h; each finished by an air cool.

### 2.2. Sample preparation

The specimen was extracted from the mid-radius section of a fully heat treated forging using electric discharge machining and standard metallographic techniques were used to polish the surface. The sample was then mounted on a stub for scanning electron microscope (SEM) imaging and focused ion beam (FIB) milling. The FIB milling step was performed in a Helios FIB/SEM at 30 kV ion acceleration voltage to produce a needle geometry approximately 400 nm in diameter at the base. The needle was attached to the top of a copper post approximately 1 mm in diameter and inserted into a Fishione 2050 on-axis single tilt holder prior to scanning transmission electron microscope (STEM) analysis. The purpose of preparing a needle geometry was to enable the acquisition of a full 180° tilt EDX series without shadowing of the detector occurring and to avoid problems associated with an increase in projected specimen thickness with tilt. Fig. 1(a) shows a low magnification high-angle annular dark field (HAADF-STEM) image of the FIB milled needle sample and the area selected for spectroscopic analysis close to the needle tip.

### 2.3. Data acquisition

EDX data were acquired using a FEI Osiris (S)TEM equipped with a high brightness 'XFEG' electron source and high efficiency X-ray detector system, comprised of four detectors in close proximity to the sample and symmetrically disposed around the optic axis of the microscope. The (S)TEM was operated at 200 kV in scanning mode (STEM), whereby the beam was focused to a spot approximately 1.5 nm wide and images were acquired by scanning the probe in a raster over a region of interest at 3 nm increments. EDX spectrum images were acquired at 5° tilt increments from −30° to +150°, and the gun lens was adjusted to produce a large current (7.8 nA) in a small probe for increased X-ray generation rate and reduced acquisition times (20 ms dwell time per pixel).

## 3. Results

### 3.1. 2D element mapping

Fig. 1(a) displays the superalloy needle prepared for 4D spectroscopic analysis. All the major peaks are identified in the summed EDX spectrum (Fig. 1(b)) and are as expected from the billet composition (Table 1). Prior to quantification of the EDX spectrum, all the element X-ray K lines, with the exception of the Al–K line, were found to satisfy the so-called 'thin film' criterion (further details are provided in the supplementary information). The calculated composition, using a standard-less Cliff–Lorimer method contained in the Tecnai Imaging and Analysis software (FEI Company), is therefore expected to have an accuracy of 5% or better. The EDX quantification is in good agreement with the billet composition as shown Fig 1(c).

Prior to analysis of the 4D dataset, conventional analysis was performed on the first spectrum image acquired with the needle at −30° tilt. Fig. 2(a) displays the HAADF STEM image of the needle approximately 170 nm and 230 nm in diameter at the top and bottom of the image respectively. Despite providing a useful measure of the specimen geometry, it is readily appreciated that there is very little compositional information contained in the HAADF image. The compositional information is instead contained in the EDX signals acquired at each pixel location in the STEM image. Selected maps, 100 × 200 pixels in size, of the major alloying elements are shown in Fig. 2(b–j). The expected microstructure of the nickel-based superalloy, comprised of a dense dispersion of $\gamma'$ precipitates in a $\gamma$ matrix, is clearly evident. The element maps show that the round $\gamma'$ precipitates are richer in nickel, aluminum, titanium and niobium than the surrounding $\gamma$ matrix. The EDX maps also show that the needle has a cap rich in titanium and niobium, representing a separate phase in the specimen. The oxygen signal is concentrated close to the surface of the needle, perhaps indicating the presence of an oxide on the surface. However, great care must be taken when interpreting the element maps of low energy X-rays (further analysis is provided in the discussion section).

The 2D EDX element maps provide a qualitative picture of the

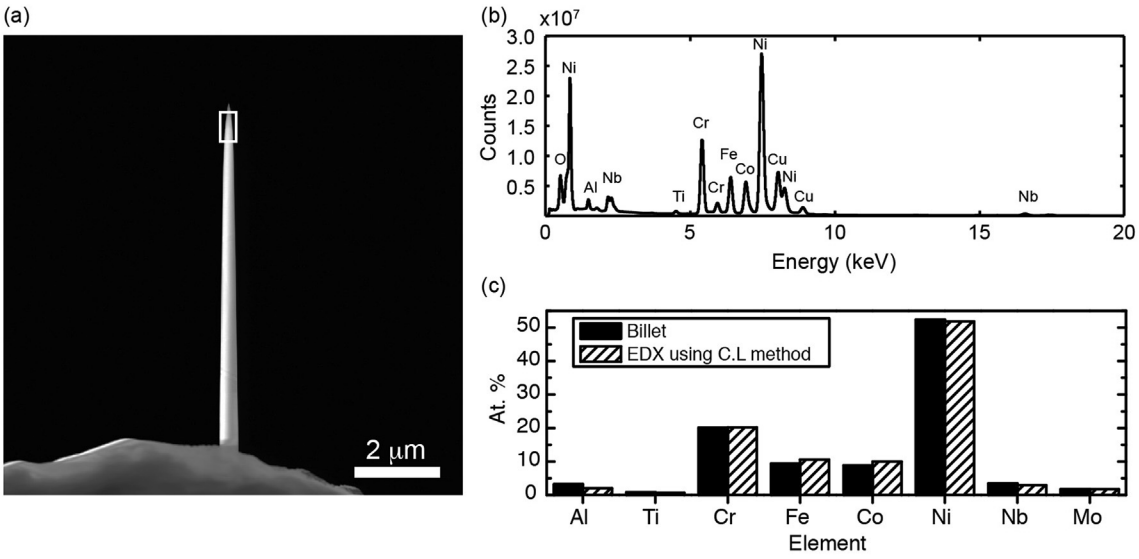


**Fig. 1.** (a) A HAADF STEM image of the FIB prepared needle specimen. The region of interest is indicated by the white box. (b) The integrated EDX spectrum of the acquired 4D dataset. (c) A comparison of the major element composition of the analyzed volume to the billet composition.

**Table 1**
The composition of the billet 718Plus superalloy [1].

| Element | Al | Ti | Cr | Fe | Co | Ni | Nb | Mo | W | C + B + P |
|---|---|---|---|---|---|---|---|---|---|---|
| wt. % | 1.45 | 0.75 | 18.0 | 9.5 | 9.1 | Bal. | 5.4 | 2.7 | 1.0 | <0.05 |

distribution of $\gamma'$ in the $\gamma$ matrix, but due to the spatial overlap of the two phases in projection, their chemical composition cannot be distinguished easily. Furthermore, it is of interest to know the size, shape and spatial distribution of $\gamma'$ in the matrix, but this information is masked in the 2D projection. Such information can, however, be recovered from a tomographic reconstruction. One could proceed in this regard by performing tomographic reconstructions of selected elements from their maps. However, it is the distribution of the different phases present that is of greater interest here. In an attempt to identify and map the different phases present, a machine learning algorithm, independent component analysis (ICA), was performed on the entire 4D dataset.

### 3.2. Independent component analysis

ICA is a blind signal separation method [19] that, in combination with principal component analysis (PCA), has been applied recently to EELS [17] and EDX [15,18,20] spectrum image data to find the compositions and distributions of multiple phases present in heterogeneous systems. The ICA algorithm solves the blind signal separation by assuming the signals to be a linear mixture of some unknown, mutually independent spectral components. Fig. 3 shows a summary of the blind signal separation analysis performed on the EDX tilt series using the HyperSpy software package [21]. First, PCA was used to reduce the dataset dimensionality to a limited number of components that account for most of the variance in the data. This was done by visual assessment of the so called 'scree plot' in Fig. 3(a), which displays the statistical variance of each component in descending order of magnitude. The plot features a distinct 'elbow' separating the first five components, labeled PC#0 to PC#4, from the remaining components, which account for a small proportion of the variability and are likely noise (see supplementary information). The first five components were retained. Second, ICA was used to compute the statistically independent spectral components (ICs) IC#0–4 (Fig. 3(b)) and their spatial loading (Fig. 3(c)) from the PCA components using the FASTICA algorithm [22] as implemented in Scikit learn [23]. The five IC spectra and their spatial loading at −30° tilt are shown in Fig. 3(c). IC#0 is rich in Ni and is concentrated in $\gamma'$ and to a lesser extent in $\gamma$. IC#1 contains strong Cr, Fe and Co peaks and is concentrated in the matrix. IC#2 only contains Cu K and L peaks and is uniformly distributed over the needle. It is interpreted as spurious signal from the supporting copper pillar or elsewhere. IC#3 contains a strong O peak and is concentrated on the needle surface. Finally, IC#4 contains a Ni-L peak. The spatial distribution of IC#4 is a close match to IC#0, however a slight reduction of intensity is observed towards the center of the needle. We interpret this component as representing the stronger absorption of Ni-L relative to Ni–K X-rays, causing the Ni-L to drop out as a separate component. All the K lines of the major alloying elements (Ni, Cr, Fe, Co) in the independent component spectra are positive, although they are not constrained to be so. IC#1 contains negative Al–K,Ti–K, Nb-L and Nb–K peaks. These seemingly unphysical negative lines appear because the matrix spectra are composed of a linear combination of IC#0 and IC#1. When appropriately weighted, the negative lines result in a reduced amount aluminum, niobium and titanium in the matrix spectra.

### 3.3. 3D reconstruction

Having identified the first five independent component spectra present above the noise in the 4D dataset, their 3D distribution was reconstructed from their spatial loadings over the 180° tilt series. First, the IC#0 maps were aligned manually using the Midas align utility in the IMOD software package. The same alignment was used for all five ICs. Next, the aligned tilt-series stacks were reconstructed in 3D using a simultaneous iterative reconstruction technique (SIRT) (implemented in the ASTRA toolbox [24]). Slices of the 3D SIRT reconstructions are displayed in Fig. 4. Common among all component reconstructions is a radial intensity gradient from the center to the surface of the needle. The gradient is likely due to the absorption of X-rays in the sample, which would be greatest for X-rays originating from the center of the needle, since these X-rays have the longest combined path length inside the sample when

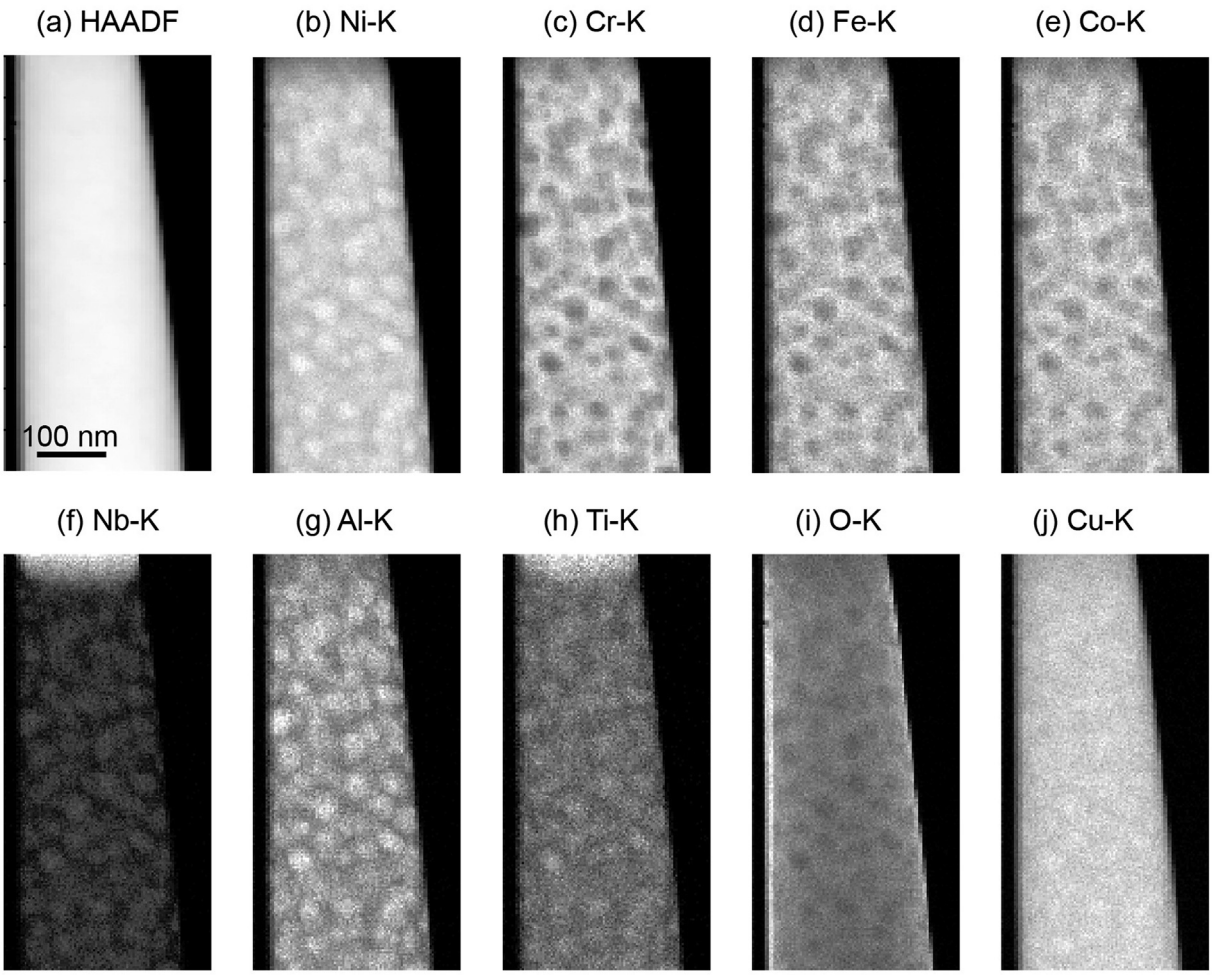


**Fig. 2.** (a) A HAADF STEM image of a region close to the tip of the needle. (b–j) 2D element maps of the major alloying elements extracted from EDX spectra.

averaged over the 180° tilt series acquisition. The γ′ precipitates are clearly visible as bright circles in the nickel rich IC#0 and IC#4 reconstructions. IC#1 has a 'Swiss-cheese' appearance, with the holes in the location of the γ′. IC#2, containing Cu K and L peaks, shows a smooth, homogeneous distribution, as one might expect if spurious in origin. Also apparent is the oxide shell in IC#3.

### 3.4. γ′ 3D morphology

The particle size, distribution, morphology and volume fraction of the γ′ strengthening phase are all important contributors to the mechanical properties of the superalloy. These critical microstructural constituents can be designed and controlled by the addition of alloying elements and appropriate heat treatments. A statistical summary of the size and shape of the segmented γ′ geometries in the sample analyzed is provided in Fig. 5. Further details on the segmentation methods are provided in the supplementary section. The particle diameter is defined as the mean length of the three principal axes of the fitted ellipsoid (Fig. 5(d)), the nearest neighbor distance is the distance between neighboring γ′ ellipsoid centroids (e), and the sphericity is the ratio of the surface area of a sphere to the surface area of the fitted ellipsoid of equal volumes (f). The γ′ size distribution approximately follows a positively skewed log-normal distribution centered at 26 nm with a standard deviation of 8.9 nm. The skewness is in contradiction to the negatively skewed size distribution predicted by Lifshitz–Slyozov–Wagner (LSW) theory for coarsening processes [25], which has formed the basis of more recent and sophisticated models that have been successfully applied to predict the growth of γ′ in nickel based superalloys [26]. This measured particle size distribution may therefore indicate that the alloy is in a transient coarsening state, which is consistent with previous work demonstrating that γ′ coarsens more slowly after thermal aging in 718Plus than in alloy 718 [27]. However, caution should be exercised as the limited spatial sampling in the acquired spectrum images (3 nm/pixel), combined with limitations in the tomographic reconstruction and segmentation steps when using a relatively large tilt increment, may compromise the accurate reconstruction of small γ′ precipitates. Their absence in the detected distribution may be sufficient to alter the shape of the secondary phase size distribution from positively to negatively skewed, and therefore we cannot confidently comment on the kinetics of the γ′ formation. The mean γ′ nearest neighbor distance is measured to be 37 ± 3 nm. The estimated volume fraction of γ′ may also suffer from limited spatial sampling and beam broadening effects, but nevertheless, we arrive at a coarse estimate of a 20 vol.% γ′ volume fraction from the segmented reconstruction.

Fig. 6 displays the measured γ′ diameter in this study compared to those found in the literature for different aging times [26–29]. Lohnert et al. [28] described the LSW-like growth of γ′ in 718Plus by measuring an average γ′ diameter of 17, 30 and 33 nm for 2, 8 and 12 h aging times respectively at 788 °C. Similar findings were made

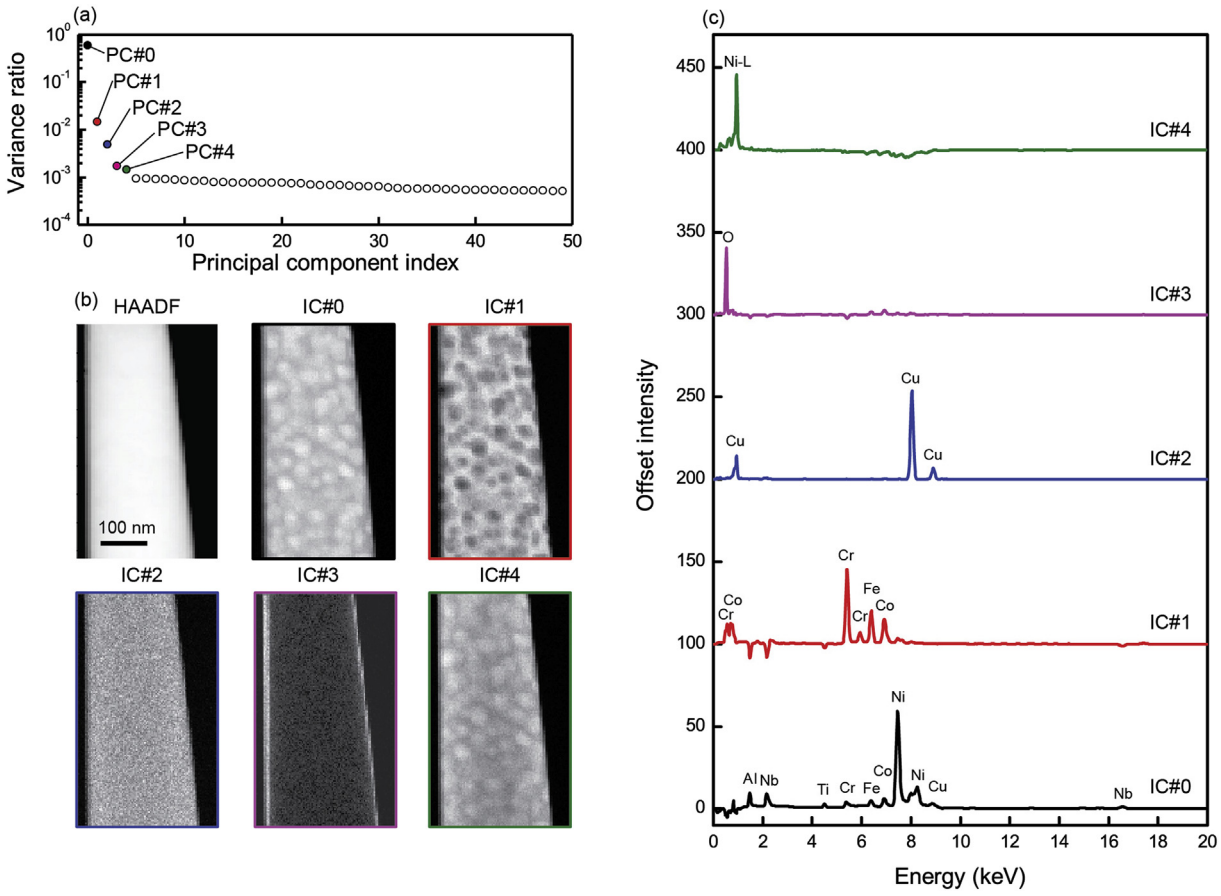


**Fig. 3.** (a) A scree plot of the fifty principal components. (b) Independent component weightings (IC#0–IC#4) at −30° tilt and their corresponding component spectra (c).

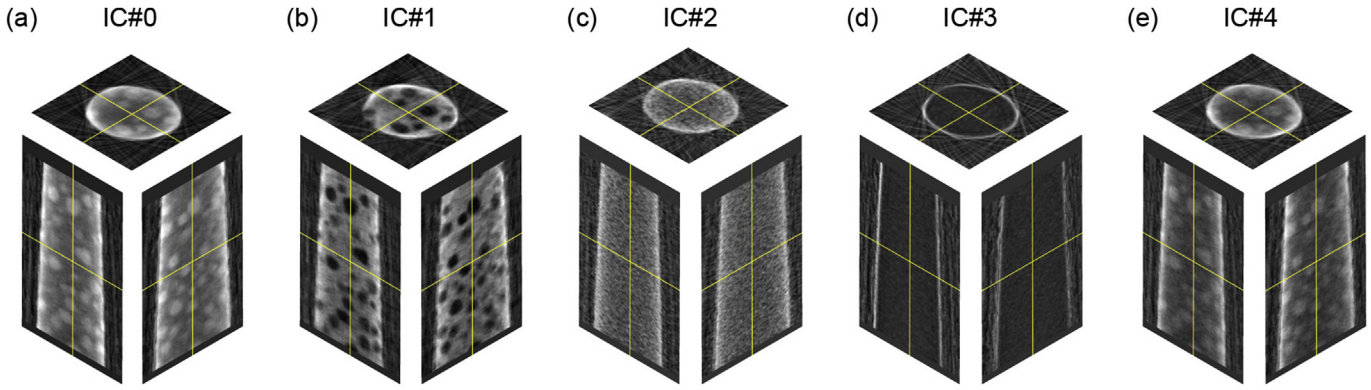


**Fig. 4.** Ortho-slices of the reconstructions of independent components IC#0–#4 (a–e).

by Srinivasan et al. for aging times of 0.1, 1, 10 h [29]. These data are in good agreement with the γ′ diameter measured in this study with the alloy aged for 8 h. For comparison a LSW-model curve was fitted to the data.

### 3.5. Composition

Upon close inspection of the IC spatial weightings, we observe that the weight of IC#1 drops to zero in the discontinuous γ′ precipitate regions, and both IC#0 and IC#1 have non-zero weightings in the continuous matrix region. The nickel-based γ matrix in 718Plus is expected to be enriched in the d-block solutes, including similarly sized Cr, Fe and Co [30]. This solute enrichment is reflected in IC#1, which contains strong Cr, Fe and Co peaks. We therefore assign IC#0 as representative of the γ′ phase, and a weighted linear mixture of IC#0 and IC#1 as representative of the γ matrix phase. We find good agreement between the compositional quantification of IC#0, calculated using the standard-less Cliff–Lorimer method contained in the Tecnai Imaging and Analysis software (Fig. 7(b)), and the composition of γ′ in a similar ALLvac 718Plus alloy obtained by APT [31]. To quantify the γ matrix, we calculated the mode of the IC#0 to IC#1 ratio in the reconstructed matrix volume (IC#0:IC#1 = 1.12), and quantified the linearly weighted spectrum, labeled IC#01, using Cliff–Lorimer method as described above

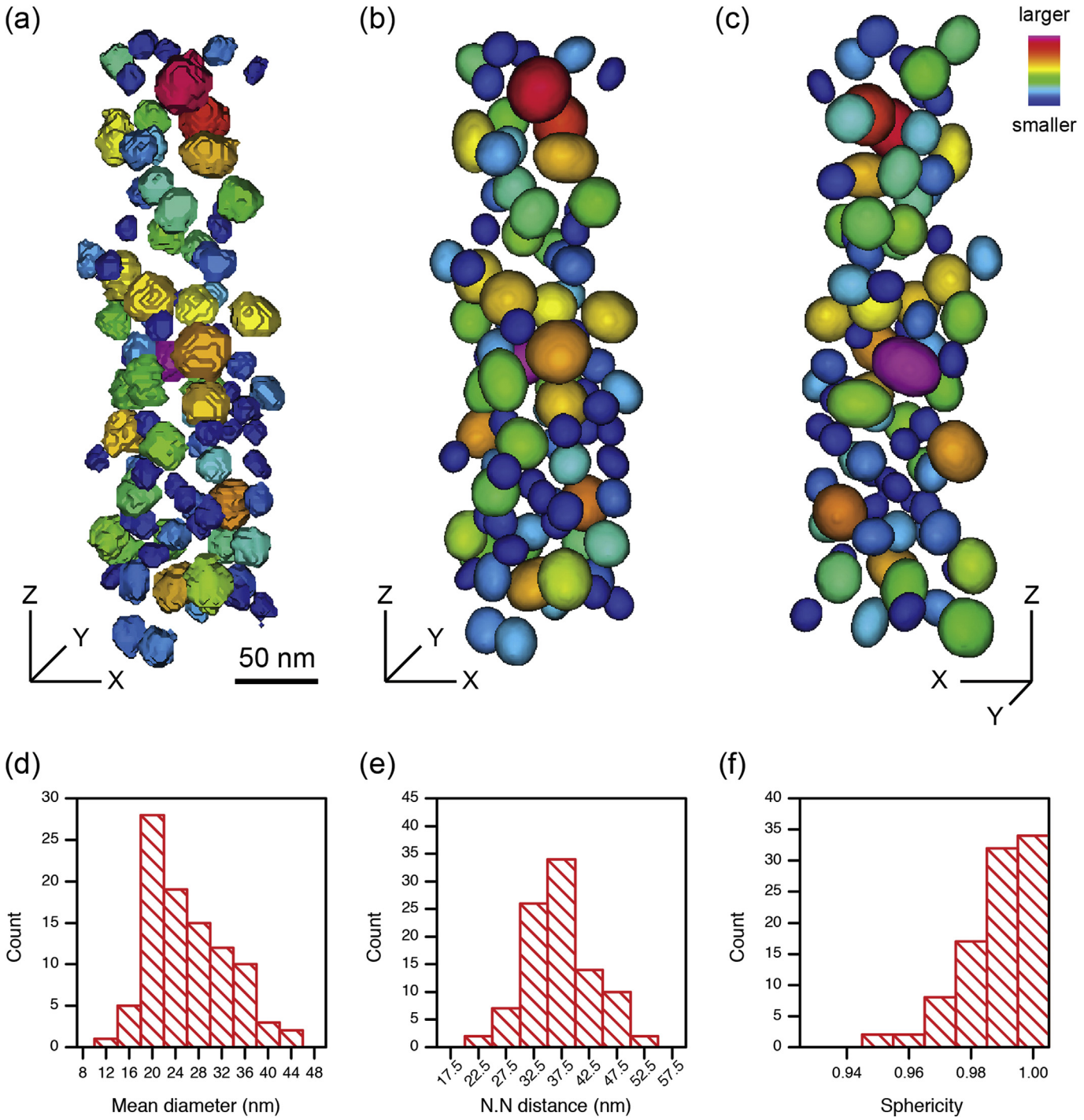


**Fig. 5.** (a–c) Segmentation and visualization of the γ′ strengthening phase (a) before and (b–c) after ellipsoid fitting. The distribution of the diameter (d) nearest neighbor distance (e) and sphericity (f) of the γ′ in the analyzed volume.

(Fig. 7(c)). We notice that, unlike IC#1, the combined spectrum IC#01 does not contain negative aluminum, titanium and niobium lines. We find a surprisingly good overall agreement between IC#0 and IC#01 and the atom probe composition of γ′ and the matrix respectively (Fig. 7(b and d)).

### 3.6. Volume fraction

If the compositions of the various phases in the alloy are known, their relative fractions can be calculated using a lever-rule based approach as shown by Blavette et al. [3]. If, for example, the element concentration differences between the γ matrix ($c\gamma$) and both the overall billet composition ($c_0$), as well as the γ′ phase compositions ($c\gamma'$) are plotted on orthogonal axes, the slope of the line of best fit passing through the origin gives the molar fraction of γ and γ′ in the alloy. Here, the compositions of γ, γ′ and the billet were extracted from components IC#0, IC#01 and the billet composition respectively (Table 1), and the η composition was extracted from a

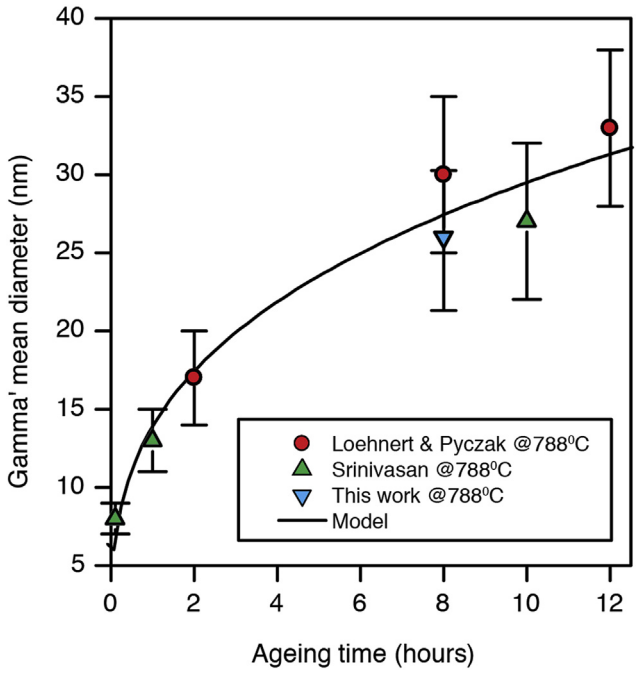


**Fig. 6.** A comparison of the measured coarsening of γ′ from the literature to this work. The error bar for this work spans the standard deviation (8.9 nm) of a fitted log normal curve to the γ′ size distribution shown in Fig. 5(d). The black line is a fitted curve following a LSW-type relationship.

**Table 2**
The experimentally determined compositions (in at.%) of the individual phases present and the overall billet composition used in the Blavette calculation.

| Phase/Element | Al | Ti | Cr | Fe | Co | Ni | Nb | Mo |
|---|---|---|---|---|---|---|---|---|
| γ′ (IC#0) | 7 | 2 | 5 | 6 | 7 | 70 | 3 | 0 |
| γ (IC#01) | 1 | 0 | 26 | 15 | 13 | 44 | 0 | 1 |
| η | 4 | 4 | 2 | 3 | 7 | 68 | 12 | 0 |
| Billet | 3 | 1 | 20 | 9 | 9 | 53 | 3 | 2 |
| Blavette method | 2 | 1 | 18 | 11 | 11 | 53 | 3 | 1 |

shows a secondary ion image of the 718Plus microstructure, obtained using a FEI Helios FIB/SEM, revealing elongated η precipitates surrounded by a precipitate free zone (PFZ), as well as a fine dispersion of round γ′ less than 100 nm in size. The η phase precipitation depends strongly on thermomechanical history, starting microstructure, degree of deformation introduced and temperature. Commonly a PFZ of up to 300 nm can be found around the circumference of η particles. This gives an indication as to how far solute atoms can travel to form η. Given an average η thickness of 300 nm and an η volume fraction content of about 10 vol.%, as estimated from Fig. 8, the depleted volume can occupy up to 30 vol.% of the alloy. For the analysis we assume that solute atoms cannot travel long distances, which seems justified due to the occurrence of PFZ and can be explained by the sluggish diffusion of Nb, which is the major solute atom here. Evidently, the sub-solvus forging and the applied pre-solution heat treatment leads to significant η precipitation, lowering the availability of solute atoms for

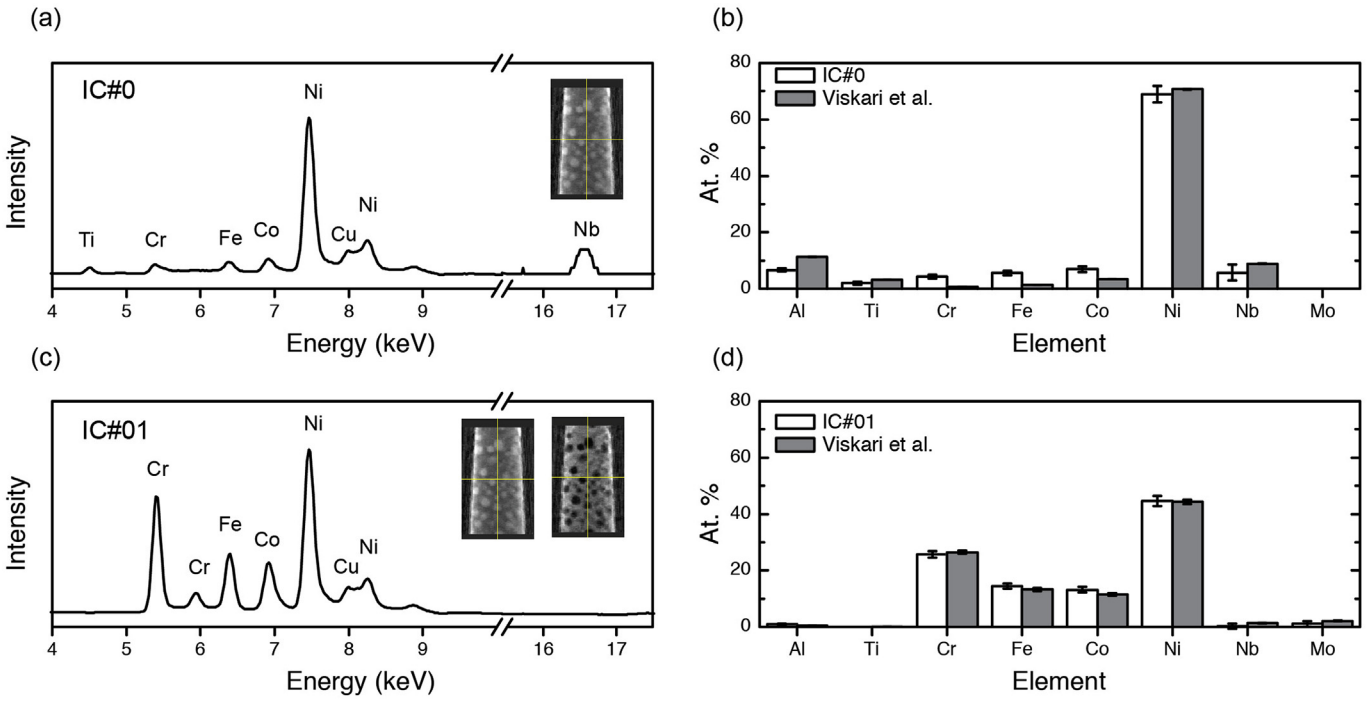


**Fig. 7.** A comparison of the composition of components IC#0 (a,b) and IC#01 (c,d) to APT determined compositions of the γ′ and γ phases in 718Plus.

separate EDX scan of a single η particle in the γ matrix. Trace alloying elements were omitted from the analysis. A summary of the compositions input into the calculation is provided in Table 2.

The γ′ volume fraction will depend on the thermal history of the 718Plus superalloy and on the amount of η phase present as both phases are competing for the same solute atoms (Nb, Al, Ti). Fig. 8 the subsequent aging step that is used to adjust γ′ precipitation. We therefore apply the Blavette method twice, once for precipitation of η in 30% of the volume and then for γ′ for the remaining 70 vol.%.

A linear trend line was used to find a least squares fit to the phase composition difference data for each precipitate and the molar fraction of the phases present was calculated from the fitted

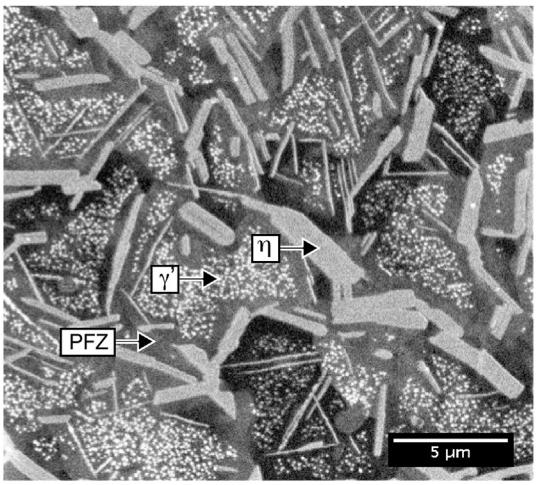


**Fig. 8.** Secondary ion image of the 718Plus microstructure, revealing elongated plate-like η precipitates surrounded by a PFZ, as well as a fine dispersion of round γ′ less than 100 nm in size.

lines (Fig. 9). The calculated molar fraction of the γ′ and η phases in the respective subset were found to be 38 at.% and 36 at.%. Corrected for the spatial independence, molar fractions for γ, γ′ and η in this alloy are 61 at.%, 28 at.% and 11 at.%, respectively. If we assume the density of the γ, γ′ and η phases in 718Plus to be 8.616, 8.277 and 8.582 g/cm$^3$, we arrive at the coarse volume fraction estimates of 62, 27 and 11 vol.% respectively. The discrepancy between the lever-rule derived γ′ volume fraction and the tomographic reconstruction volume estimate of γ′ (27 vs. 20 vol.%) may be in part due to the limited spatial sampling in the data acquisition. Small γ′ particles may not be reconstructed faithfully, thus leading to an underestimate of the γ′ volume fraction in the reconstructed volume. Furthermore, the reconstructed volume may not accurately reflect the average volume fraction of γ′ in the alloy. Srinivasan et al. [29] analyzed superalloy samples aged for 0.1, 1.0 and 10.0 h at 788 °C and found increasing γ′ volume fractions of 0.2, 5 and 15 vol.% respectively. If the different aging times are taken into account, the trends in these data are consistent with our measurements. The calculated overall composition (the molar fraction weighted phase composition sum) is also in good agreement with the overall billet composition (Table 2).

## 4. Discussion

In this section, a justification of the methodology used and the implications and limitations of the results and further interpretation is provided. Included is a discussion on the use of ICA, EDX quantification and the composition of γ′. All of these steps involve some bias and error to varying degrees, and as such they must be performed with care.

### 4.1. Independent component analysis

The use of ICA greatly simplified the qualitative analysis of the multi-phase needle composition, providing a quick identification of phases present in the alloy. The compositions of components IC#0 and IC#01 are in good agreement with APT compositions of the γ′ and γ matrix phases respectively. ICA has separated Cu as a component (IC#2), which is believed to be spurious, likely originating from the Cu support post. This separation demonstrates that ICA may be helpful for the quantification of copper containing alloys, as the spurious copper signal may be separable from true signal from the sample, provided the copper shows spatial inhomogeneity. Similarly, the separation of a surface oxide layer (IC#3) may aid the quantification of a bulk oxide. This outcome provides a simpler interpretation of the extracted components than PCA of EDX spectra, which are often difficult to interpret [32]. A further advantage of the use of the combination of PCA and ICA is noise reduction. The component maps, by the very nature of ICA, inherently have reduced noise compared to element maps extracted from X-ray peak intensities or peak areas [14], which is important for subsequent 3D reconstruction and segmentation.

### 4.2. EDX quantification

Performing quantitative X-ray microanalysis is known to be a non-trivial exercise and can be particularly challenging when analyzing second phase precipitates in a multicomponent system. Furthermore, the undesirable effects of electron beam broadening and X-ray absorption in the sample are expected to be appreciable in the relatively thick needle. However, thicker samples are desirable for 3D volumetric analysis, to capture sample features

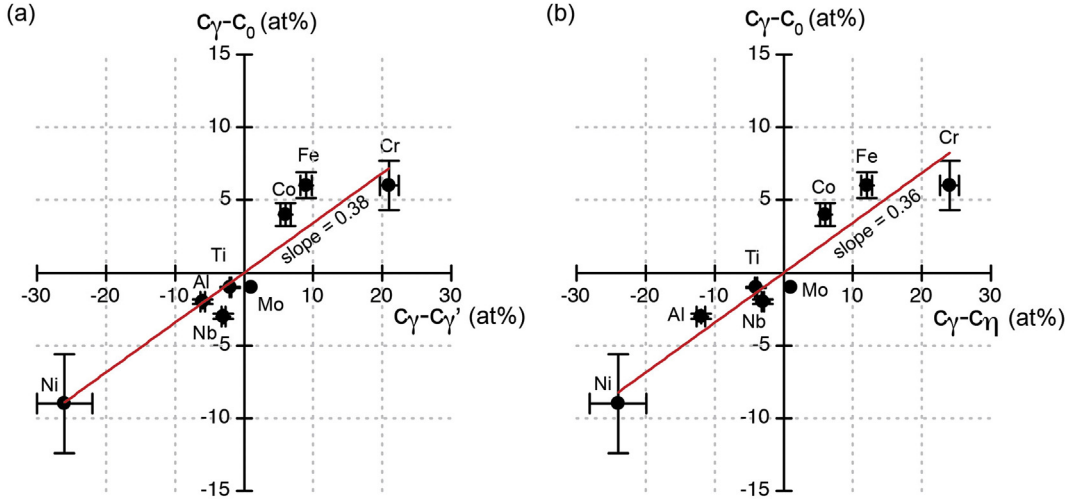


**Fig. 9.** A graphical representation of the Blavette method for determining phase fractions in the superalloy. The fitted lines have slopes of (0.38, 0.36), which lead to calculated molar fractions for (γ, γ′, η) of (61, 28, 11) at%.

sufficiently. Thus a compromise between the two factors must be made. In order to capture a statistically significant number of γ′ precipitates in the matrix, a sample thickness of approximately 200 nm was deemed suitable. Over a sample thickness of 200 nm, an experimental convergence semi-angle of 15 mrad results in a purely geometric beam spread of 6 nm in diameter at exit surface of the sample. In addition, elastic scattering of the electron beam in the sample results in further broadening, calculated to be 18 nm midway through a 200 nm thick foil of pure nickel at 200 kV. While the broadening is likely to deteriorate the quality of both the 2D spectrum images and the tomographic reconstructions, its effect may be limited due to the full 180° acquisition, which will average the beam spread over the needle volume. The effects of X-ray absorption on EDX quantification are described in more detail in the supplementary section.

### 4.3. Composition of γ′

Of particular interest is the extraction of the γ′ composition from the superalloy, which is obscured in conventional 2D analysis due to the signal mixing of X-rays from the surrounding matrix. In this study, the ICA treatment of the EDX spectrum image tilt series appears to have captured the composition of γ′ in component IC#0. Furthermore, we have obtained the spectrum of the matrix, IC#01, by linearly combining IC#0 and IC#1. The reconstructed voxel intensities of IC#0 centered in the γ′ phase show appreciable variation from one γ′ to the next (SI Fig. 1(b)). It appears as though the main contribution to this variation is due to X-ray absorption, causing signals emerging from the center of the needle to have reduced intensity upon detection. It has been shown elsewhere that the composition of the γ′ precipitates in a similar superalloy system can vary with size [33], however, the compositional variation was found to extend over a much larger range of precipitate sizes than those studied here.

## 5. Conclusions

The application of the ICA blind signal separation method has proven to be a powerful method for obtaining information on the phases present in an advanced nickel-based superalloy, in particular the γ′ strengthening phase. Traditionally, heterogeneous nanoscale materials are difficult to quantify because analytical signals from the different phases present can overlap in projection and detection. However, under the right conditions, blind signal separation algorithms can separate the mixed signals into the separate components that may be representative of the individual phases present. At the same time, the decomposition of a large dataset into a limited number of components reduces the size of the dataset, which can significantly speed up data analysis and the 3D reconstruction of the phases present in the material. In this work, the composition of the ICA component spectra representing the γ and γ′ phases are in excellent agreement with APT data. It is likely that the technique described here may be used on a variety of materials systems. Primarily, it is best to analyze a sample thin enough such that the detected X-ray signals meet the thin-film criterion. For tomography, this implies that a compromise must be met in the choice of sample thickness analyzed. The analyzed volume should be thin enough to satisfy the thin film criterion, but also thick enough to enable sufficient sampling of a 3D volume to justify the use of tomography.

## Acknowledgments

The research leading to these results has received funding from the European Union Seventh Framework Programme under Grant Agreement 312483 – ESTEEM2 (Integrated Infrastructure Initiative-I3), as well as from the European Research Council under the European Union's Seventh Framework Programme (FP/2007–2013)/ERC grant agreement 291522 - 3DIMAGE. D.R. acknowledges support from the Royal Society's Newton International Fellowship scheme. RKL acknowledges a Junior Research Fellowship at Clare College. RK acknowledges financial support from Rolls-Royce, EPSRC and the BMWi under EP/H022309/1, EP/H500375/1 and grant number 20T0813. F.d.l.P. and C.D. acknowledge funding from the ERC under grant no. 259619 PHOTO EM. Special thanks to Giorgio Divitini and Lech Staniewicz for preparation of the FIB needle specimen and to Stephen A Croxall for SEM/FIB imaging.

## Appendix A. Supplementary data

Supplementary data related to this article can be found at http://dx.doi.org/10.1016/j.actamat.2016.01.042.

## References

[1] R.L. Kennedy, Allvac 718Plus, superalloy for the next forty years, Superalloys 718 (2005) 1–14, 625, 706 Var. Deriv.
[2] S. Ochiai, Y. Oya, T. Suzuki, Alloying behaviour of Ni3Al, Ni3Ga, Ni3Si and Ni3Ge, Acta Metall. 32 (1984) 289–298.
[3] D. Blavette, E. Cadel, B. Deconihout, The role of the atom probe in the study of nickel-based superalloys, Mater. Charact. 44 (2000) 133–157.
[4] D.J. De Rosier, a. Klug, Reconstruction of three dimensional structures from electron micrographs, Nature 217 (1968) 130–134.
[5] P.A. Midgley, M. Weyland, 3D electron microscopy in the physical sciences: the development of Z-contrast and EFTEM tomography, Ultramicroscopy 96 (2003) 413–431.
[6] R. Leary, P.A. Midgley, J.M. Thomas, Recent advances in the application of electron tomography to materials chemistry, Acc. Chem. Res. 45 (2012) 1782–1791.
[7] G. Möbus, R.C. Doole, B.J. Inkson, Spectroscopic electron tomography, Ultramicroscopy 96 (2003) 433–451.
[8] Z. Saghi, X. Xu, Y. Peng, B. Inkson, G. Möbus, Three-dimensional chemical analysis of tungsten probes by energy dispersive X-ray nanotomography, Appl. Phys. Lett. 91 (2007) 251906.
[9] K. Lepinay, F. Lorut, R. Pantel, T. Epicier, Chemical 3D tomography of 28nm high K metal gate transistor: STEM XEDS experimental method and results, Micron 47 (2013) 43–49.
[10] A. Genc, L. Kovarik, M. Gu, H. Cheng, P. Plachinda, L. Pullan, et al., XEDS STEM tomography for 3D chemical characterization of nanoscale particles, Ultramicroscopy 131 (2013) 24–32.
[11] T.J.A. Slater, P.H.C. Camargo, M.G. Burke, N.J. Zaluzec, S.J. Haigh, Understanding the limitations of the Super-X energy dispersive X-ray spectrometer as a function of specimen tilt angle for tomographic data acquisition in the S/TEM, J. Phys. Conf. Ser. 522 (2014) 012025.
[12] B. Goris, L. Polavarapu, S. Bals, G. Van Tendeloo, L.M. Liz-Marzán, Monitoring galvanic replacement through three-dimensional morphological and chemical mapping, Nano Lett. 14 (2014) 3220–3226.
[13] G. Haberfehlner, A. Orthacker, M. Albu, J. Li, G. Kothleitner, Nanoscale voxel spectroscopy by simultaneous EELS and EDS tomography, Nanoscale 6 (2014) 14563–14569.
[14] B. Goris, S. Turner, S. Bals, G. Van Tendeloo, Three-dimensional valency mapping in ceria nanocrystals, ACS Nano 8 (2014) 10878–10884.
[15] G. Lucas, P. Burdet, M. Cantoni, C. Hebert, Multivariate statistical analysis as a tool for the segmentation of 3D spectral data, Micron 52–53 (2013) 49–56.
[16] C. Parish, L. Brewer, Multivariate statistics applications in phase analysis of STEM-EDS spectrum images, Ultramicroscopy 110 (2010) 134–143.
[17] F. de la Peña, M.-H. Berger, J.-F. Hochepied, F. Dynys, O. Stephan, M. Walls, Mapping titanium and tin oxide phases using EELS: an application of independent component analysis, Ultramicroscopy 111 (2011) 169–176.
[18] D. Rossouw, P. Burdet, F. de la Peña, C. Ducati, B.R. Knappett, A.E.H. Wheatley, P.A. Midgley, Multicomponent signal unmixing from nanoheterostructures: overcoming the traditional challenges of nanoscale X-ray analysis via machine learning, Nano Lett. (2015), 150317074024002.
[19] C. Jutten, J. Herault, Blind separation of sources, part I: an adaptive algorithm based on neuromimetic architecture, Signal Process. 24 (1991) 1–10.
[20] P. Kotula, M. Keenan, Application of multivariate statistical analysis to STEM X-ray spectral images: interfacial analysis in microelectronics, Microsc. Microanal. (2006) 538–544.
[21] Francisco de la Peña, Pierre Burdet, Tomas Ostasevicius, Mike Sarahan, Magnus Nord, Vidar Tonaa Fauske, Josh Taillon, Alberto Eljarrat, Stefano Mazzucco, Gaël Donval, Luiz Fernando Zagonel, Michael Walls, Iygr, Hyperspy: HyperSpy 0.8.2, 2015, http://dx.doi.org/10.5281/zenodo.28025.

[22] E. Bingham, A. Hyvärinen, A fast fixed-point algorithm for independent component analysis of complex valued signals, Int. J. Neural Syst. 10 (2000) 1–8.
[23] F. Pedregosa, G. Varoquaux, A. Gramfort, V. Michel, B. Thirion, O. Grisel, et al., Scikit-learn: machine learning in python, J. Mach. Learn. Res. 12 (2011) 2825–2830.
[24] W. Palenstijn, K.J. Batenburg, J. Sijbers, The ASTRA tomography toolbox, in: Proc. 13th Int. Conf. Comput. Math. Methods Sci. Eng. C, 2013.
[25] I. Lifshitz, V. Slyozov, The kinetics of precipitation from supersaturated solid solutions, J. Phys. Chem. Solids 19 (1961) 35–50.
[26] A. Baldan, Progress in Ostwald ripening theories and their applications to nickel-base superalloys. Part I: Ostwald ripening theories, J. Mater. Sci. 37 (2002) 2171–2202.
[27] X. Xie, G. Wang, J. Dong, C. Xu, W.-D. Cao, R. Kennedy, Structure stability study on a newly developed nickel-base superalloy – Allvac 718Plus, Superalloys 718 (2005) 179–191, 625, 706 Var. Deriv.
[28] K. Löhnert, F. Pyczak, Microstructure evolution in the nickel base superalloy Allvac® 718PlusTM, Superalloys 718 (2010) 877–891, 625, 706 Var. Deriv.
[29] D. Srinivasan, L.U. Lawless, E.A. Ott, Experimental determination of TTT diagram for alloy 718Plus®, in: Superalloys International Symposium, 2012, pp. 759–768.
[30] R.C. Reed, The Superalloys, University Press, Cambridge, 2006. http://dx.doi.org/10.1017/CBO9780511541285.
[31] L. Viskari, K. Stiller, Atom probe tomography of Ni-base superalloys Allvac 718Plus and Alloy 718, Ultramicroscopy 111 (2011) 652–658.
[32] M.G. Burke, M. Watanabe, D.B. Williams, J.M. Hyde, Quantitative characterization of nanoprecipitates in irradiated low-alloy steels: advances in the application of FEG-STEM quantitative microanalysis to real materials, J. Mater. Sci. 41 (2006) 4512–4522.
[33] Y.Q. Chen, T.J.A. Slater, E.A. Lewis, E.M. Francis, M.G. Burke, M. Preuss, S.J. Haigh, Measurement of size-dependent composition variations for gamma prime (γ′) precipitates in an advanced nickel-based superalloy, Ultramicroscopy 144 (2014) 1–8.